

Observation of uniaxial strain tuned spin cycloid in a freestanding BiFeO₃ film

Zhe Ding,^{1,2,3,*} Yumeng Sun,^{1,2,3,*} Ningchong Zheng,^{4,5,6,7,*} Xingyue Ma,^{4,5,6,7,*}
Mengqi Wang,^{1,2,3} Yipeng Zang,^{4,5,6,7} Pei Yu,^{1,2,3} Pengfei Wang,^{1,2,3} Ya Wang,^{1,2,3}
Yurong Yang,^{4,5,6,7,†} Yuefeng Nie,^{4,5,6,7,‡} Fazhan Shi,^{1,2,3,8} and Jiangfeng Du^{1,2,3,§}

¹CAS Key Laboratory of Microscale Magnetic Resonance and School of Physical Sciences,
University of Science and Technology of China, Hefei 230026, China

²CAS Center for Excellence in Quantum Information and Quantum Physics,
University of Science and Technology of China, Hefei 230026, China

³Hefei National Laboratory, University of Science and Technology of China, Hefei 230088, China

⁴National Laboratory of Solid State Microstructures, Nanjing University, Nanjing 210093, China

⁵Jiangsu Key Laboratory of Artificial Functional Materials, Nanjing University, Nanjing 210093, China

⁶College of Engineering and Applied Science, Nanjing University, Nanjing 210093, China

⁷Collaborative Innovation Center of Advanced Microstructures, Nanjing University, Nanjing 210093, China

⁸School of Biomedical Engineering and Suzhou Institute for Advanced Research,
University of Science and Technology of China, Suzhou 215123, China

Non-collinear spin order that breaks space inversion symmetry and allows efficient electric-field control of magnetism makes BiFeO₃ a promising candidate for applications in low-power spintronic devices[1–4]. Epitaxial strain effects have been intensively studied and exhibit significant modulation of the magnetic order in BiFeO₃[5, 6], but tuning its spin structure with continuously varied uniaxial strain is still lacking up to date. Here, we apply *in situ* uniaxial strain to a freestanding BiFeO₃ film and use scanning NV microscope to image the nanoscale magnetic order in real-space. The strain is continuously increased from 0% to 1.5% and four images under different strains are acquired during this period. The images show that the spin cycloid tilts by $\sim 12.6^\circ$ when strain approaches 1.5%. A first principle calculation has been processed to show that the tilting is energetically favorable under such strain. Our *in situ* strain applying method in combination with scanning NV microscope real-space imaging ability paves a new way in studying the coupling between magnetic order and strain in BiFeO₃ films.

Antiferromagnetic material is robust against external magnetic field disturb, has super-fast spin dynamics and possesses large magneto-transport effects. Due to the merits above, antiferromagnetic materials have important application in spintronics and other magnetism-based techniques [7]. Although it is a promising material, because of its anti-parallel spin configuration which leads to zero stray-field, antiferromagnetic material cannot be well studied by normal near-field imaging techniques [8]. Non-collinear antiferromagnetic perovskite compound bismuth ferrite (BiFeO₃, BFO) is the only magnetoelectric multiferroic material under room temperature. Since the non-collinear spin cycloid breaks spatial inversion symmetry, it can be controlled by external electric field and thus costs much less energy comparing to ordinary ferromagnetic devices [8]. BFO owns spin cycloid because of the Dzyaloshinskii–Moriya interaction (DMI), such cycloid induces an effective magnetization which is too weak to detect with normal methods such as MFM[9] and PEEM[10]. At the same time, since BFO has ~ 2.7 eV bandgap[11], sp-STM also lacks the ability to perform imaging. Scanning NV microscopy (SNVM) is an emergent real-space scanning

method with nanoscale spatial resolution and $\mu\text{T}/\sqrt{\text{Hz}}$ magnetic sensitivity[12, 13]. People have utilized SNVM to study the magnetic structure of BFO epitaxial films at nanoscale [6, 8, 14].

BFO is a kind of perovskite compound while fulfills noncentrosymmetric rhombohedral $R3c$ space group[16]. The structure of BFO is shown in figure 1(c), for the sake of brevity, we adopt pseudo-cubic unit cell. In each unit cell, bismuth atoms are at eight corners, while at the center lays the iron atom contained by an octahedron constructed by six oxygen atoms. The ferroelectric Curie temperature of BFO is 1103 K[17, 18], below which the ferroelectric polarization is as high as $100 \mu\text{C}/\text{cm}^2$ in high quality grown films [19, 20]. The antiferromagnetic order of BFO is characterized as G-type, with Néel temperature $T_N = 683 \text{ K}$ [21]. 3d electrons of Fe³⁺ are the origin of magnetism of BFO, while ferroelectricity and antiferrodistortive break the spatial inversion symmetry which gives rise to a DMI. This interaction leads to a small canting angle between neighbor spins and this produces an effective spin density as large as $0.02 \mu_B$ per unit cell [8, 22]. Under proper conditions, spin distribution in BFO will turn cycloidal, which is an incommensurable periodic order. A cycloidal order can be described by a wave vector \mathbf{k} , as indicated in figure 1(c). The magnetic order of BFO is decided by external field, strain, temperature, size and more factors, while the effect of strain has been intensively studied[5, 6, 23–26]. Previous works utilized different substrates to adjust the epitaxial strain in

* These authors contributed equally to this work.

† yangyr@nju.edu.cn

‡ ynie@nju.edu.cn

§ djf@ustc.edu.cn

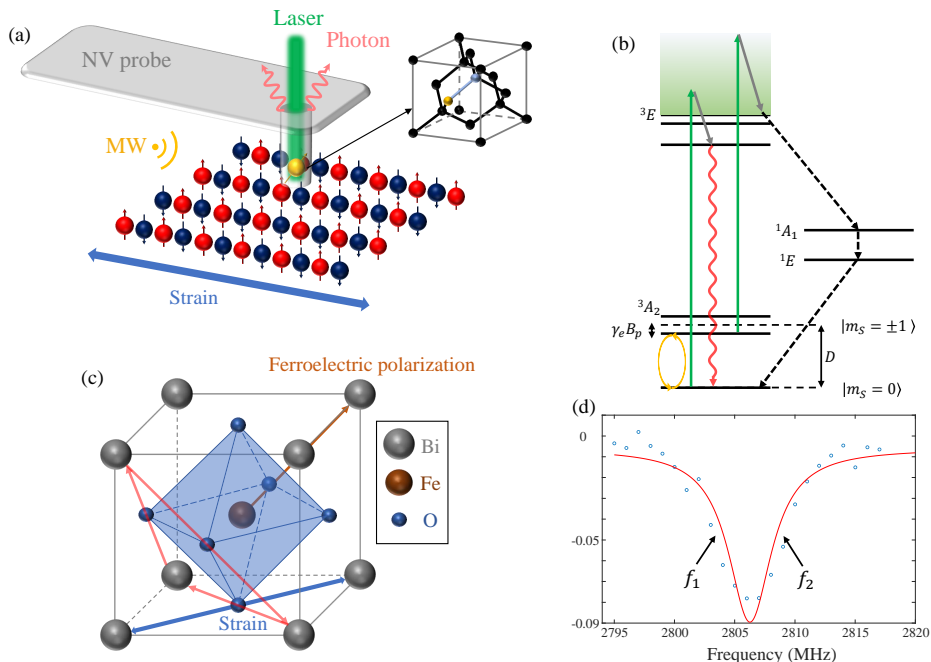


Figure 1. Principle of the experiment. (a) The sketch of an SNVM setup. An NV is at the tip of the probe while its structure is shown in the inset. Under the NV probe, blue and red ball array stands for the antiferromagnetic material imaged during the experiment. Continuous uniaxial strain (blue two-way arrow) is applied *in situ* with an organic substrate (not shown in the sketch). (b) The energy level structure of an NV center. (c) The structure of a BFO pseudo-cubic unit cell. The ferroelectric state has been polarized along [111] beforehand (brown arrow) and the uniaxial strain (blue two-way arrow) is applied along [110], which is paralleled to the polarization's projection to the plane. Possible cycloidal wave vectors (light red arrows) in bulk BFO are along face diagonals perpendicular to ferroelectric polarization. (d) The demonstration of dual-iso-B protocol. CW-ODMR data are collected at two frequencies ($f_{1,2}$) [15].

BFO and found two types of cycloidal order[5, 6]. While these researches provide the phase diagram of BFO magnetic order with respect to epitaxial strain, they are not able to impose adjustable strain to BFO *in situ* and this leaves the mechanism of BFO magnetic transformation at critical point an outstanding open question [5, 6, 16]. Besides, previous researches mainly focus on biaxial strain while real-space imaging of magnetic structure under uniaxial strain has not yet been performed.

In this work, we adopt a new method base on molecular beam epitaxy (MBE) to prepare freestanding BFO film[20, 27]. A 75-unit-cell-thick BFO (001) film is prepared and transferred to organic substrate Polyethylenaphthalate(PEN) while epoxy is used as the glue to conduct strain to the BFO film. During experiments, **uniaxial, continuous and *in situ*** strain is imposed on the BFO film by means of mechanically stretching the PEN substrate [28, 29]. In principle, this method is able to impose arbitrary in-plane tensile strain on the film, while in this work the strain principal axis deviates from [110] by $\sim 4.7^\circ$. Such strain breaks the intrinsic $R3c$ symmetry of BFO and provide a way to tune the spin cycloid's direction continuously. A home-built SNVM is used to perform nanoscale magnetic imaging of its stray field. By using this method, we find that the direction

of the cycloidal order is modulated by the uniaxial strain which confirms to a first principle calculation. This phenomenon may help people understanding the transition mechanism of magnetic order under strain[5, 16] whilst the freestanding film based method can be used in strain-based spintronics, new heterostructure devices and other new multifunctional devices [20, 28, 29]. Our new freestanding film based method in combination with SNVM real-space imaging ability paves a new way to study strain-magnetism coupling in antiferromagnetic materials.

SNVM has been widely used in condensed matter physics[30–35], here we apply SNVM to the freestanding BFO film to acquire stray field distribution near the surface. The structure of our SNVM setup is demonstrated in figure 1(a). The Nitrogen-Vacancy color center (NV center) in diamond is a point defect shown in the inset. It is formed by a nitrogen atom (orange ball in the inset) and an adjacent vacancy (blue ball in the inset) in diamond lattice [36]. As shown in figure 1(b), the NV center is pumped from ground state (3A_2) into phonon sideband by 532 nm green laser (green arrows) and relaxes into excited state (3E) with angular momentum conserved (grey arrows). $|m_S = 0\rangle$ emits photons (wavy red arrow) during the transition to ground state

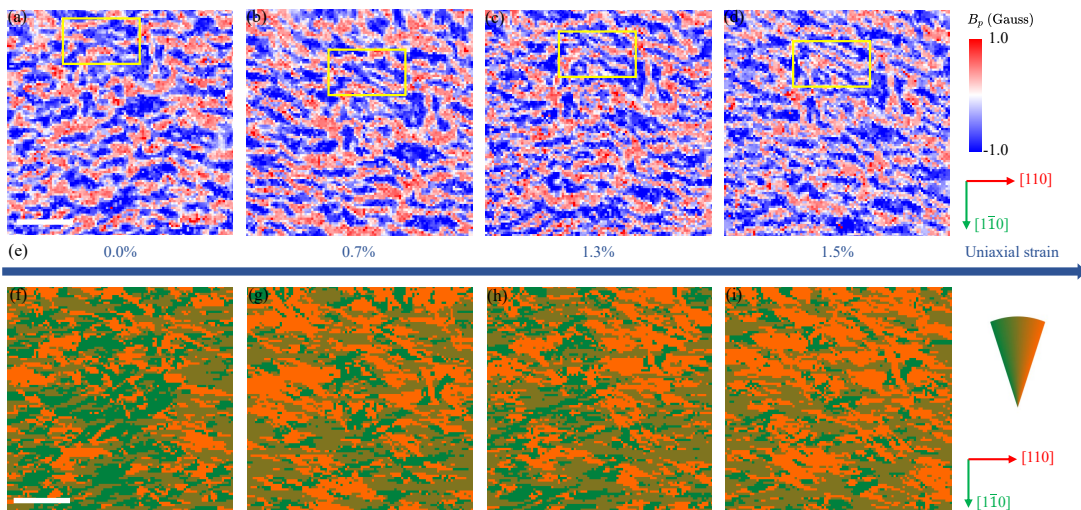


Figure 2. Spin cycloid variation in real-space during the increasing of strain. (a-d) Images of stray field B_p under different strains. The white scale bar corresponds to 500 nm, a direction reference of $[1\bar{1}0]$ and $[110]$ is displayed to the right. Yellow boxes highlight a local transition of the spin cycloid. (e) The sketch of applied strains corresponding to stray field images above. (f-i) Wave vector direction in real-space under different strains. The white scale bar corresponds to 500 nm. The fan-shaped colorbar demonstrates the wave vector direction under the frame displayed by green and red arrows below.

and the photons are finally detected by a single photon detector. $|m_S = \pm 1\rangle$ evolves into ground state through meta-stable states ($^1A_1, ^1E$) with no detectable photon emitted (black dotted line arrows). The degeneracy of $|m_S = \pm 1\rangle$ is lifted by Zeeman splitting generated by external magnetic field ($\gamma_e B_p$) and resonant microwave (MW, orange circled arrow) is applied by a copper micro-antenna to selectively excite one of the spin states. By using the photon count rate's difference between $|m_S = 0\rangle$ and $|m_S = \pm 1\rangle$, it is straight forward to readout the NV center's spin state.

In our experiment, by applying green laser and MW simultaneously and readout the photon counts, we utilize the Continuous Wave Optically Detected Magnetic Resonance (CW-ODMR) spectrum. In order to accelerate the imaging speed, we adopt the dual-iso-B protocol shown in figure 1(d) [8]. Applying this protocol, by sampling at two MW frequencies, we are able to calculate the projection of the stray field to the NV axis [15]. By scanning across a magnetic film edge, we determine that the distance from the NV center to sample surfaces is 78.5 ± 1.8 nm (with 95% confidence) [15, 37, 38].

Beforehand, a piezoelectric force microscope (PFM) is utilized to electrically polarize an area of the BFO film to $[111]$ [15]. During the experiment, a uniaxial strain is applied to the BFO film via the PEN substrate. By employing X-ray diffraction (XRD) after the experiment, we are able to calibrate strains under which the images are acquired [15].

SNVM imaging is implemented under four different strains: $\epsilon = 0.0\%$, 0.7% , 1.3% , 1.5% , the results are shown in figure 2. The principal axis of strain deviates from high symmetry direction $[110]$ by 4.7° , which breaks $R3c$ symmetry and leads to cycloid tilting. From the

real-space imaging one can find that although the coherence length is relatively small, the sample does possess local cycloidal order, which is modulated by the increasing uniaxial strain. We attribute this small coherence length to in-homogeneous strain gradient introduced by epitaxial interface [39]. Be aware that we are using a novel, organic and soft substrate in combination with a freestanding film to realize *in situ* strain tuning. Without rigid constraint from crystal substrates, freestanding films possess intrinsic unevenness, which may also lead to the small coherence length [28]. Despite the relatively small coherence length, spin cycloid's variation during the increasing of strain is rather distinct. We calculate the direction of cycloidal wave vector by minimizing variances on segments parallel to different directions and apply region growing algorithm to the results to acquire wave vector direction domain image plotted in figure 2(f-i). It is evident that during the application of strain, the wave vector tilts away from $[1\bar{1}0]$.

Be aware that the applied strain also modulates local distribution of the magnetic order, there are plural non-trivial local transitions while the applied strain increases. For example, by retracing with respect to tomography markers and magnetic patterns, we are able to determine that the boxed areas in figure 2 are at the same spot [40]. Two different ordered areas at this spot merge into one when strain approaches 1.5%. This phenomenon is interpreted as the release of local strain gradient under external strain.

We have acquired a qualitative result that during the application of strain, the wave vector tilts away from $[1\bar{1}0]$. In order to obtain quantitative relation between the tilting angle and strain, we apply Fourier transformation (FT) to the initial and final real-space scanning

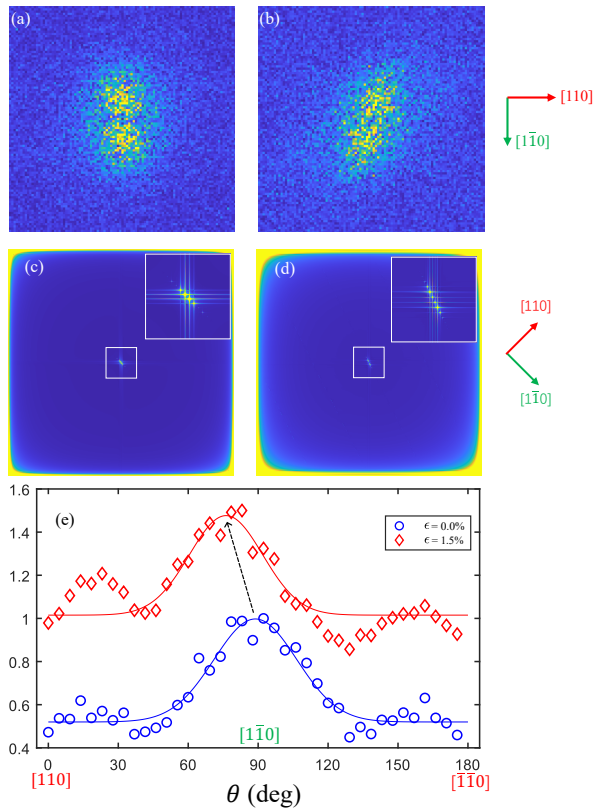


Figure 3. Reciprocal space analysis. (a,b) The FT results of real-space stray field image. (a) corresponds to stray field under no strain and (b) under 1.5% strain. The reference frame is displayed with green and red arrows to the right. (c,d) The FT results of first principle calculation. (c) is calculated with no strain applied and (d) a 1.5% uniaxial strain along a direction deviates from pseudo-cubic $[110]$ by 4.7° . The insets are enlarged picture of the boxed area close to origin for the sake of clarity of details. The reference frame of the calculation is plotted to the right. (e) Counted results of the distribution of the cycloidal wave vector under different strains with respect to azimuth angle. High lattice orientations are labelled at corresponding azimuth angles. Blue circles and red diamonds stands for data under 0.0% and 1.5% strain respectively. Gaussian fit for both peaks are displayed with solid lines according to which there is a tilting angle as large as 12.6° .

results to obtain the wave vector distribution in reciprocal space, which is shown in figure 3(a,b). It is distinctive that the wave vector tilts away from $[1\bar{1}0]$ while the strain increases, this confirms to our qualitative result from the real-space imaging. We accounts the wave vector with respect to its azimuth angle, the result is displayed in figure 3(e). One can find that, while the strain increases, the wave vector tilts by $\sim 12.6^\circ$.

In order to explain the wave vector's tilting under strain, first-principle-based simulations are performed using magnetic effective Hamiltonian [15, 41] with the magnetic exchange interaction coefficients evaluated from the four-state mapping approach [42].

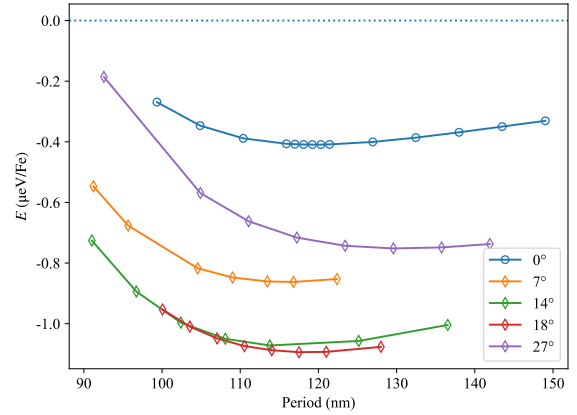


Figure 4. Energy curves with respect to cycloidal period. Data of cycloidal order with wave vector parallel to $[1\bar{1}0]$ are shown with blue circles. Data with wave vectors along different directions (7° , 14° , 18° , 27° away from $[1\bar{1}0]$) are shown with diamonds in different colors. The values are given by the energy differences with respect to the antiferromagnetic state, which is denoted by the horizontal dotted lines. The solid lines between symbols are only guided eyes.

The uniaxial strain is modeled by stretching the cell along the direction slightly deviates from pseudo-cubic $[110]$ direction by 4.7° . The strain is chosen to be 1.5% according to XRD calibration, and an estimated Poisson's ratio of about 0.24 calculated via XRD data is also considered [15]. Note that due to the symmetry broken caused by strain, the symmetry of the system is reduced from space group $R3c$ to $P1$, and all the sixfold-degenerate pair in the $R3c$ structure[41] are no longer degenerate. The calculated exchange coefficients are shown in the Supplemental Information [15].

Parallel tempering Monte Carlo (PTMC) simulations [43, 44] are performed to solve the magnetic effective Hamiltonian. A large supercell of $\sqrt{2}na \times \sqrt{2}b \times c$ ($n = 2, 3, \dots, 300$) is used study the cycloidal phase, where \mathbf{a} is along the pseudo-cubic $[1\bar{1}0]$ direction, \mathbf{b} is along the pseudo-cubic $[110]$ direction, and \mathbf{c} is along the pseudo-cubic $[001]$ direction. To study the stable period of the cycloidal phase, energy per Fe atom is calculated as a function of cycloidal period, as shown in Fig. 4. This energy-versus-period curve shows a minimum at 119 nm, which is similar to that in the $R3c$ phase [41].

To study cycloid which deviates the $[1\bar{1}0]$ direction, several *oblique* supercells are constructed. The supercells slightly tilting about \mathbf{c} direction were used. The angle between the lattice vector \mathbf{a} and the pseudo-cubic $[110]$ direction is used to define the oblique angle of cycloid. For example, one of the oblique supercells used in this work is defined by $\mathbf{a} = 211\mathbf{a}_0 - 165\mathbf{b}_0$, $\mathbf{b} = 7\mathbf{a}_0 + 9\mathbf{b}_0$, $\mathbf{c} = \mathbf{c}_0$ where \mathbf{a}_0 , \mathbf{b}_0 and \mathbf{c}_0 are the vectors we used to define our relaxed $R3c$ BFO lattices which are close to the pseudo-cubic $[100]$, $[010]$ and $[001]$ direction, respectively. The oblique angle of such cell is then the angle between the \mathbf{a}

and $\mathbf{a}_0 - \mathbf{b}_0$, that is approximately 7° . Figure 4 shows the calculated energy of supercells with different oblique angles as functions of cycloidal period. The energies of supercells with non-zero oblique angles are lower than that of supercells without oblique angle, indicating the oblique supercells are more energetically favorable. Moreover, with the increasing of the oblique angle from 0° , the energy shows a nonmonotonic behavior with respect to the oblique angle, with a minimum around 18° . Such value is in very well consistent with the measured value 12.6° (refer to figure 3(e)).

To confirm the cycloids in the rotated supercells do propagate along a direction deviates from $[1\bar{1}0]$, FT is also performed to the PTMC simulation results [15]. Figure 3 (d) shows the spectrum of one supercell with oblique angle 18° after the FT, showing a peak at the coordinate (12, -6), which is away from the pseudo-cubic $[1\bar{1}0]$ direction by 18° (calculated from $45^\circ - \arctan(6/12)$). On the other hand, figure 3 (c) shows such spectrum on a supercell without oblique angle of non-stretched cell ($R3c$ phase as in Ref. [41]), showing a peak at the coordinate (10, -10), which is exactly along the pseudo-cubic $[1\bar{1}0]$ direction. The deviation of such peak from pseudo-cubic $[1\bar{1}0]$ direction definitely confirms that the cycloids in oblique cells do propagate along a direction deviates from $[1\bar{1}0]$ direction. We thus conclude that such deviation of the cycloid is energetically more favorable than without deviation.

Note that we also performed above analysis on BFO at tensile strain of 0.5% along *exactly* the pseudo-cubic $[110]$ direction without oblique angle, and found the cycloid propagates along the pseudo-cubic $[1\bar{1}0]$ (i.e. with oblique angle 0°) is the most energetically favored phase. Such fact indicates that the deviation of the cycloid propagation originates from the symmetry broken caused by the uniaxial strain colored with an oblique angle.

In summary, we apply continuous *in situ* uniaxial strain to freestanding BFO films and scan the magnetic stray field near surface with SNVM. A modulation of di-

rection of the magnetic order is found and a first principle calculation is conducted. The first principle calculation result confirms that the strain induced magnetic effective Hamiltonian evolution is responsible for the rotation of magnetic order. This result is helpful for people to understand the mechanism of magnetic order transformation under strains. Besides, our freestanding-film-based *in situ* strain applying method paves a new way to study the coupling between strain and magnetism in antiferromagnetic materials. With some slight improvements, it is possible to conduct arbitrary in-plane tensile strain to the sample, which provides people with higher degrees of freedom to study the mechanism of magnetic order transition under strains.

ACKNOWLEDGMENTS

This work was supported by the National Natural Science Foundation of China (grant nos. 81788101, T2125011, No.12104447), the National Key R&D Program of China (grant nos. 2018YFA0306600 and 2021YFA1400400), the CAS (grant nos. XDC07000000, GJJSTD20200001, QYZDY-SSW-SLH004, Y201984, YSBR-068), Innovation Program for Quantum Science and Technology (Grant No. 2021ZD0302200, 2021ZD0303204), the Anhui Initiative in Quantum Information Technologies (grant no. AHY050000), the Natural Science Foundation of Jiangsu Province (grant No. BK20200262), Hefei Comprehensive National Science Center, China Postdoctoral Science Foundation (Grant No. 2020M671858) and the Fundamental Research Funds for the Central Universities.

We are grateful to the HPC resources of Nanjing University for the calculations. The NV scanning probe was provided by CIQTEK and the assembling was completed by Ruijie Shao. This work was partially carried out at the USTC Center for Micro and Nanoscale Research and Fabrication.

-
- [1] Kimura, T. *et al.* Magnetic control of ferroelectric polarization. *Nature* **426**, 55–58 (2003).
 - [2] Lottermoser, T. *et al.* Magnetic phase control by an electric field. *Nature* **430**, 541–544 (2004).
 - [3] Cheong, S.-W. & Mostovoy, M. Multiferroics: A magnetic twist for ferroelectricity. *Nature Materials* **6**, 13–20 (2007).
 - [4] Heron, J. T. *et al.* Deterministic switching of ferromagnetism at room temperature using an electric field. *Nature* **516**, 370–373 (2014).
 - [5] Sando, D. *et al.* Crafting the magnonic and spintronic response of BiFeO₃ films by epitaxial strain. *Nature Materials* **12**, 641–646 (2013).
 - [6] Haykal, A. *et al.* Antiferromagnetic textures in BiFeO₃ controlled by strain and electric field. *Nature Communications* **11**, 1704 (2020).
 - [7] Baltz, V. *et al.* Antiferromagnetic spintronics. *Reviews of Modern Physics* **90**, 015005 (2018).
 - [8] Gross, I. *et al.* Real-space imaging of non-collinear antiferromagnetic order with a single-spin magnetometer. *Nature* **549**, 252 (2017).
 - [9] Hartmann, U. Magnetic Force Microscopy. *Annual Review of Materials Science* **29**, 53–87 (1999).
 - [10] Locatelli, A. & Bauer, E. Recent advances in chemical and magnetic imaging of surfaces and interfaces by XPEEM. *Journal of Physics: Condensed Matter* **20**, 093002 (2008).
 - [11] Sando, D. *et al.* Large elasto-optic effect and reversible electrochromism in multiferroic BiFeO₃. *Nature Communications* **7**, 1–7 (2016).
 - [12] Taylor, J. M. *et al.* High-sensitivity diamond magnetometer with nanoscale resolution. *Nature Physics* **4**, 810–816 (2008).
 - [13] Maletinsky, P. *et al.* A robust scanning diamond sen-

- sor for nanoscale imaging with single nitrogen-vacancy centres. *Nature Nanotechnology* **7**, 320–324 (2012).
- [14] Chauleau, J.-Y. *et al.* Electric and antiferromagnetic chiral textures at multiferroic domain walls. *Nature Materials* **19**, 386–390 (2020).
- [15] Please refer to supplementary information.
- [16] Burns, S. R., Paull, O., Juraszek, J., Nagarajan, V. & Sando, D. The Experimentalist’s Guide to the Cycloid, or Noncollinear Antiferromagnetism in Epitaxial BiFeO₃. *Advanced Materials* **32**, 2003711 (2020).
- [17] Kaczmarek, W., Pająk, Z. & Polomska, M. Differential thermal analysis of phase transitions in (Bi_{1-x}Lax)FeO₃ solid solution. *Solid State Communications* **17**, 807–810 (1975).
- [18] Neaton, J. B., Ederer, C., Waghmare, U. V., Spaldin, N. A. & Rabe, K. M. First-principles study of spontaneous polarization in multiferroic BiFeO₃. *Physical Review B* **71**, 014113 (2005).
- [19] Wang, J. *et al.* Epitaxial BiFeO₃ Multiferroic Thin Film Heterostructures. *Science* **299**, 1719–1722 (2003).
- [20] Ji, D. *et al.* Freestanding crystalline oxide perovskites down to the monolayer limit. *Nature* **570**, 87–90 (2019).
- [21] Kiselev, S. V., Ozerov, R. P. & Zhdanov, G. S. Detection of Magnetic Order in Ferroelectric BiFeO₃ by Neutron Diffraction. *Soviet Physics Doklady* **7**, 742 (1963).
- [22] Albrecht, D. *et al.* Ferromagnetism in multiferroic BiFeO₃ films: A first-principles-based study. *Physical Review B* **81**, 140401 (2010).
- [23] Waterfield Price, N. *et al.* Strain Engineering a Multiferroic Monodomain in Thin-Film BiFeO₃. *Physical Review Applied* **11**, 024035 (2019).
- [24] Sando, D. *et al.* A magnetic phase diagram for nanoscale epitaxial BiFeO₃ films. *Applied Physics Reviews* **6**, 041404 (2019).
- [25] Sando, D. *et al.* Influence of flexoelectricity on the spin cycloid in (110)-oriented BiFeO₃ films. *Physical Review Materials* **3**, 104404 (2019).
- [26] Chen, Z. *et al.* Complex strain evolution of polar and magnetic order in multiferroic BiFeO₃ thin films. *Nature Communications* **9**, 3764 (2018).
- [27] Lu, D. *et al.* Synthesis of freestanding single-crystal perovskite films and heterostructures by etching of sacrificial water-soluble layers. *Nature Materials* **15**, 1255–1260 (2016).
- [28] Zang, Y. *et al.* Giant Thermal Transport Tuning at a Metal/Ferroelectric Interface. *Advanced Materials* **34**, 2105778 (2022).
- [29] Han, L. *et al.* Giant Uniaxial Strain Ferroelectric Domain Tuning in Freestanding PbTiO₃ Films. *Advanced Materials Interfaces* **7**, 1901604 (2020).
- [30] Zhe Ding, Fazhan Shi & Jiangfeng Du. Nanoscale magnetic imaging based on quantum sensing with diamond and its applications to condensed matter physics. *Physics* **49**, 359–372 (2020).
- [31] Casola, F., van der Sar, T. & Yacoby, A. Probing condensed matter physics with magnetometry based on nitrogen-vacancy centres in diamond. *Nature Reviews Materials* **3**, 17088 (2018).
- [32] Tetienne, J.-P. *et al.* Nanoscale imaging and control of domain-wall hopping with a nitrogen-vacancy center microscope. *Science* **344**, 1366–1369 (2014).
- [33] Pelliccione, M. *et al.* Scanned probe imaging of nanoscale magnetism at cryogenic temperatures with a single-spin quantum sensor. *Nature Nanotechnology* **11**, 700–705 (2016).
- [34] Hedrich, N. *et al.* Nanoscale mechanics of antiferromagnetic domain walls. *Nature Physics* **1–4** (2021).
- [35] Ku, M. J. H. *et al.* Imaging viscous flow of the Dirac fluid in graphene. *Nature* **583**, 537–541 (2020).
- [36] Doherty, M. W. *et al.* The nitrogen-vacancy colour centre in diamond. *Physics Reports* **528**, 1–45 (2013). 1302.3288.
- [37] Jenkins, A. *et al.* Single-spin sensing of domain-wall structure and dynamics in a thin-film skyrmion host. *Physical Review Materials* **3**, 083801 (2019).
- [38] Tetienne, J.-P. *et al.* The nature of domain walls in ultrathin ferromagnets revealed by scanning nanomagnetometry. *Nature Communications* **6**, 6733 (2015).
- [39] Sando, D. *et al.* Interfacial Strain Gradients Control Nanoscale Domain Morphology in Epitaxial BiFeO₃ Multiferroic Films. *Advanced Functional Materials* **30**, 2000343 (2020).
- [40] When we adjust strain, a movement at hundred micrometer scale is introduced by the strain applying positioner. A built-in optical microscope supplies tomography information to help reset the sample’s position. The limited spatial resolution of the optical microscope is the reason that the field of views under different strains slightly mismatch, though we could retrace common areas by referring to neighbor magnetic patterns.
- [41] Xu, C., Xu, B., Dupé, B. & Bellaiche, L. Magnetic interactions in bifeo₃: A first-principles study. *Phys. Rev. B* **99**, 104420 (2019).
- [42] Xiang, H., Lee, C., Koo, H.-J., Gong, X. & Whangbo, M.-H. Magnetic properties and energy-mapping analysis. *Dalton Trans.* **42**, 823–853 (2013).
- [43] Earl, D. J. & Deem, M. W. Parallel tempering: Theory, applications, and new perspectives. *Phys. Chem. Chem. Phys.* **7**, 3910–3916 (2005).
- [44] Lou, F. *et al.* Pasp: Property analysis and simulation package for materials. *The Journal of Chemical Physics* **154**, 114103 (2021).

Supplemental information

Observation of uniaxial strain tuned spin cycloid in a freestanding BiFeO₃ film

I. RECONSTRUCTING STRAY FIELD FROM DUAL-ISO-B DATA

In the main text, we mentioned that CW-ODMR is utilized to acquire the stray field imaging near BFO surface, this section explains the principle of CW-ODMR and dual-iso-B protocol.

In this paragraph, while analyzing NV electron ODMR, we utilize NV local frame. NV axis is defined as z-axis and spin states along z-axis are taken as basis: $\{|+1\rangle_e, |0\rangle_e, |-1\rangle_e\}$. The operator of electron spin's z-component is:

$$S_z = \begin{pmatrix} 1 & 0 & 0 \\ 0 & 0 & 0 \\ 0 & 0 & -1 \end{pmatrix}. \quad (1)$$

NV centers utilized in the experiment are prepared by ¹⁵N ion implanting followed by annealing under 900 °C. Noting that an ¹⁵N's nuclear spin quantum number is 1/2, by taking spin states along z direction $\{|+1/2\rangle_n, |-1/2\rangle_n\}$ as basis, the operator of nuclear spin's z-component is

$$I_z = \frac{1}{2} \begin{pmatrix} 1 & 0 \\ 0 & -1 \end{pmatrix}. \quad (2)$$

Consider the Hilbert space of NV electron and nuclear spin, we could write the Hamiltonian under secular approximation:

$$H_{NV} = DS_z^2 - \gamma_e B_z S_z + A_N S_z I_z. \quad (3)$$

In this formula, B_z is the external magnetic field's projection on z direction, while $D = 2870$ MHz is the zero-field splitting; $\gamma_e = 2.8$ MHz/Gauss is the gyromagnetic ration of electron; $A_N = 3.03$ MHz is ¹⁵N's hyperfine coupling strength. During the experiment, we only collected the data of resonance between $|+1\rangle_e$ and $|0\rangle_e$. By calculating the eigenvalues of the Hamiltonian, one can find that with respect to the nuclear spin states, there are two resonant frequencies: $f_{\pm} = D - \gamma_e B_z \pm A_N/2$. In the CW experiment, for each frequency, two sets of data are collected: one set is the photon count $C(f)$ under MW and pump laser; the other set is the photon count C_0 under pump laser without MW. By taking these two sets of data, we define the CW spectrum: $S(f) := C(f)/C_0 - 1$. It has been proven that this spectrum is Lorentzian[1]. The nuclear spin is under mixed state $\rho_n = 1/2(|+1/2\rangle_n\langle+1/2| + |-1/2\rangle_n\langle-1/2|)$ so the spectrum is the superposition of two Lorentzian lines:

$$S(f, B_z) = - \left[\frac{A}{(f - f_+(B_z))^2/\Delta^2 + 1} + \frac{A}{(f - f_-(B_z))^2/\Delta^2 + 1} \right], \quad (4)$$

in which A, Δ are contrast and half width at half maximum of one Lorentzian line and calibrated before the experiment.

Under the dual-iso-B mode, we only collect data at two frequency points $S_i = S(f_i, B_z), i = 1, 2$, in order to acquire a relatively high sensitivity, we take $f_1 = f_- - \Delta, f_2 = f_+ + \Delta$. Notice that experiment data at each frequency point provides a quartic algebraic equation with respect to B_z , we can locate the solution B_z by comparing solution sets under two frequency points. It is necessary to point out that in order to lift the degeneracy between $|\pm 1\rangle_e$, external magnetic field \mathbf{B}_{ext} is applied and the solved B_z above is the superposition of the external magnetic field and stray field $B_z = B_{\text{ext},z} + B_{\text{str},z}$. Since \mathbf{B}_{ext} has been calibrated beforehand, it is straightforward to acquire the stray field by subtracting it from the solved magnetic field.

II. CALIBRATING NV HEIGHT

By scanning across ferromagnetic film's edges, we are able to acquire the information about the height of the NV center[2, 3]. Under the reference frame shown in FIG.1(a), the stray field of a ferromagnetic film magnetized along z axis distributes according to the formula below:

$$B_x = \frac{\mu_0 M_s t}{2\pi} \frac{h}{(x - x_0)^2 + h^2}, \quad (5)$$

$$B_z = -\frac{\mu_0 M_s t}{2\pi} \frac{x}{(x - x_0)^2 + h^2}. \quad (6)$$

In this formula, h is the height of NV, M_s, t are saturation magnetization and thickness of the ferromagnetic film respectively. x_0 is the position of the edge of the film and μ_0 is the vacuum permeability. Since the experiment data is $B_p = \mathbf{B} \cdot \mathbf{n}_{NV}$, by applying the formula above, one can calculate h by fitting B_p .

We proceed line scan across the edge of ferromagnetic film Ta(5 nm)/CoFeB(1 nm)/MgO(1.2 nm)/Ta(2 nm) and fit the B_p data to calculate the NV height. The data is shown in FIG.1(b) and the fitting results shows that the NV height is 78.5 ± 1.8 nm (with 95% confidence).

III. ELECTRIC POLARIZATION OF BFO

Piezoelectric force microscopy (PFM) has been utilized to electrically polarize the BFO film along [111] before experiments and LPFM has been used to confirm that BFO has indeed been polarized. Results of the PFM are shown in FIG.2.

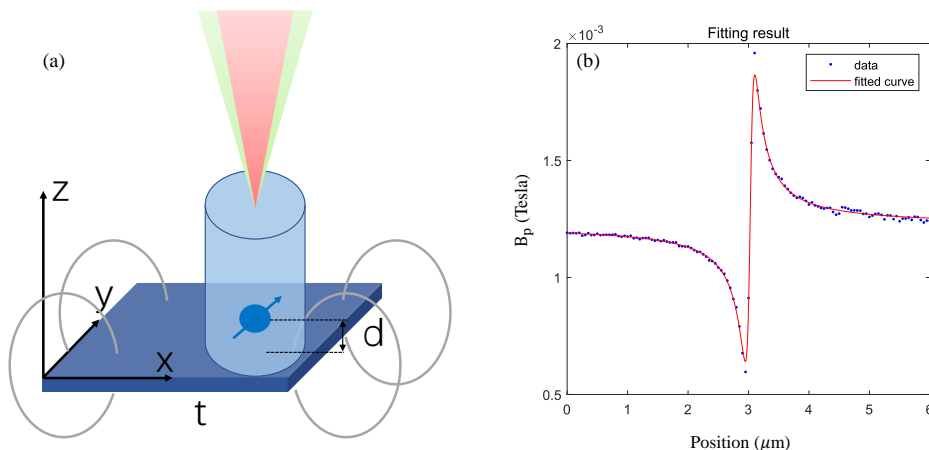


FIG. 1: Calculating NV height. (a) is the layout of the experiment for the height calculation. (b) is the line scan and fitting results.

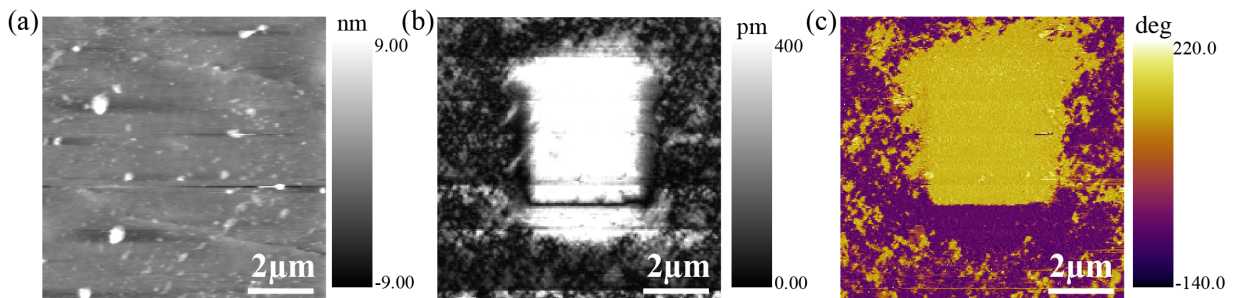


FIG. 2: PFM results. (a), (b) and (c) are topography, amplitude and phase data respectively.

IV. STRAIN CALIBRATION AND STRUCTURE ANALYSIS

Strains under which the experiments have been performed are calibrated by X-ray diffraction (XRD) afterwards. During experiments, stretching lengths of the substrate ΔL are measured by the strain applying positioner's sensor and a nominal strain $\varepsilon_n = \Delta L/L \times 100\%$ is defined. Here, L is the length of the substrate. SNVM scanning in the main text are performed under $\varepsilon_n = 0.0, 1.5, 3.0, 4.5\%$. The $2\theta-\omega$ scans under different nominal strains are displayed in FIG.3.

One can calculate the lattice parameters by fitting the $2\theta-\omega$ data. The relation between lattice parameters a, b, c and nominal strain is shown in FIG.4(a). We define lat-

tice variations:

$$\delta_a = \frac{a - a_0}{a_0} \times 100\%, \quad (7)$$

$$\delta_b = \frac{b - b_0}{b_0} \times 100\%, \quad (8)$$

$$\delta_c = \frac{c - c_0}{c_0} \times 100\%. \quad (9)$$

Here, a_0, b_0, c_0 are the lattice parameters under zero nominal strain. There is a inflection point after nominal strain approaches 4.5%. After that point, microcracks appears so that the strain starts to relax [4].

For brevity, we only consider the in-plane strain and the strain tensor under principal axis coordinate is

$$\begin{pmatrix} \epsilon & 0 \\ 0 & \sigma\epsilon \end{pmatrix} \quad (10)$$

in which ϵ is the strain component under the stretching direction (corresponding to strain mentioned in the main

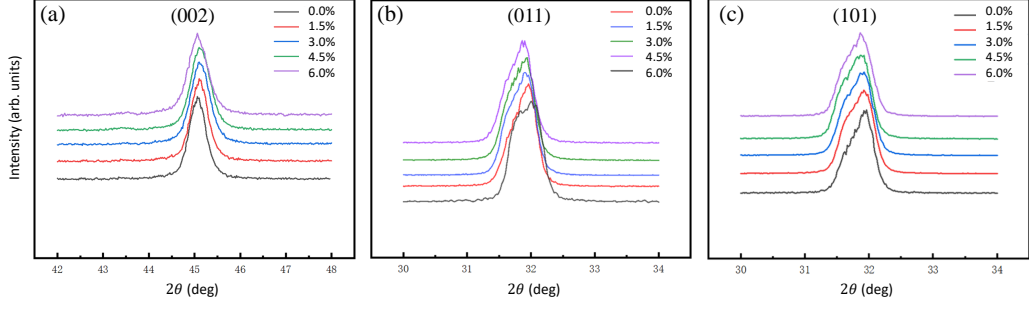


FIG. 3: 2θ - ω scans of the BFO films under different nominal strain. (a),(b),(c) are diffraction patterns of (002), (011) and (101) planes respectively.

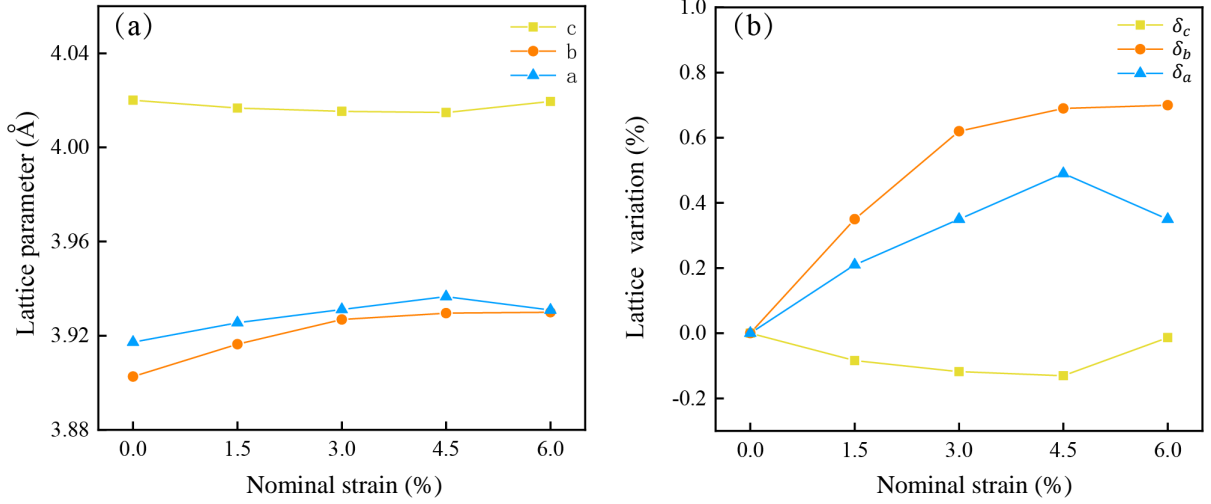


FIG. 4: (a) is the relation between lattice parameters and nominal strain. (b) is the relation between lattice variation and nominal strain.

text) and σ represents for Poisson's ratio. We transform the coordinate so that the first axis is parallel to lattice vector \mathbf{a}

$$\begin{pmatrix} \cos \theta_a & -\sin \theta_a \\ \sin \theta_a & \cos \theta_a \end{pmatrix} \begin{pmatrix} \epsilon & 0 \\ 0 & \sigma \epsilon \end{pmatrix} \begin{pmatrix} \cos \theta_a & \sin \theta_a \\ -\sin \theta_a & \cos \theta_a \end{pmatrix} = \begin{pmatrix} u_{aa} & u_{aa'} \\ u_{a'a} & u_{a'a'} \end{pmatrix} \quad (11)$$

Here, θ_a is the rotation angle of the coordinate transformation, a' labels the direction perpendicular to \mathbf{a} . It can be proven that

$$u_{aa} = \delta_a. \quad (12)$$

Note that the pseudo-cubic structure is broken by strain, a' is not necessarily parallel lattice vector \mathbf{b} . By observing the 1,1-term of the strain tensor, we could acquire the relation between strains and lattice variation δ_a . By performing a similar transformation so that the first axis

is parallel to lattice vector \mathbf{b} , we derive such equations:

$$\epsilon(\cos^2 \theta_a + \sigma \sin^2 \theta_a) = \delta_a, \quad (13)$$

$$\epsilon(\cos^2 \theta_b + \sigma \sin^2 \theta_b) = \delta_b. \quad (14)$$

Since strain changes the angle γ between \mathbf{a} and \mathbf{b} , we shall calculate γ from XRD data. In fact, one can acquire this angle by calibrating the change of ϕ between (101) and (011) interference patterns. Since the stretching direction does not deviate from [110] much, we could acquire an approximate equation of strain with respect to γ

$$\frac{1 + \sigma \epsilon}{1 + \epsilon} = \frac{\tan \gamma/2}{\tan \gamma_0/2}. \quad (15)$$

Combine equation (13), (14), (15) and note that geometric relation $\theta_a + \theta_b = \gamma$ provides another constraint, we are able to solve $\theta_a, \theta_b, \epsilon$ and σ at the same time (shown in FIG.5).

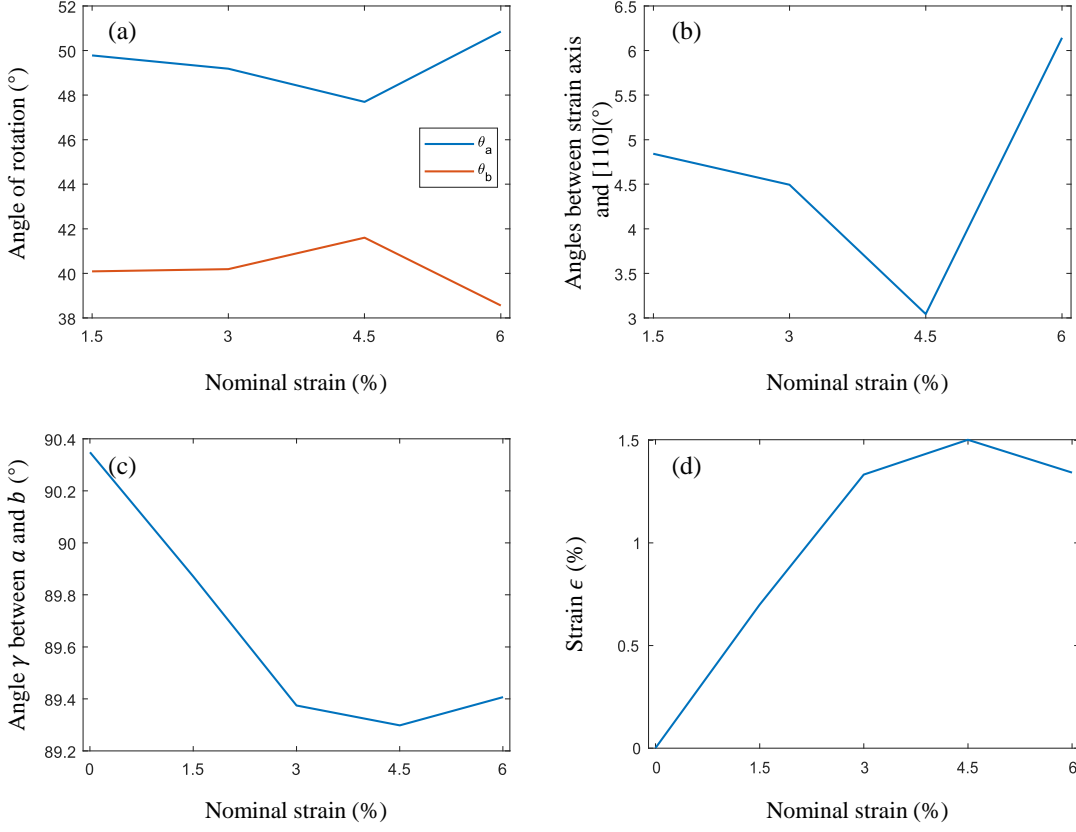


FIG. 5: Analysis results from XRD data. (a) Coordinate rotation angles mentioned in equation (13) and (14). (b) Strain deviating angle from high symmetry direction [110]. (c) Angle γ between lattice vectors \mathbf{a} and \mathbf{b} calculated from XRD data. (d) Relation between strain ϵ and nominal strain calculated from XRD data.

V. FIRST PRINCIPLE CALCULATION RESULTS

In the first principle calculation, we adopt such a magnetic effective Hamiltonian:

$$E = E_{\text{ex}} + E_{\text{dm}} + E_{\text{ani}}, \quad (16)$$

which are exchange interaction, Dzyaloshinskii-Moriya interaction (DMI) and single ion anisotropy (SIA) respectively. The forms of the three components are:

$$E_{\text{ex}} = \frac{1}{2} \sum_{\langle i,j \rangle} \mathbf{S}_i \cdot \mathcal{J}_{\langle i,j \rangle} \cdot \mathbf{S}_j, \quad (17)$$

$$E_{\text{dm}} = \frac{1}{2} \sum_{\langle i,j \rangle} \mathbf{D}_{\langle i,j \rangle} \cdot (\mathbf{S}_i \times \mathbf{S}_j), \quad (18)$$

$$E_{\text{ani}} = \sum_i \mathbf{S}_i \cdot \mathcal{A}_i \cdot \mathbf{S}_i. \quad (19)$$

Here, \mathbf{S}_i is the spin operator at site i , $\mathcal{J}_{\langle i,j \rangle}$ and $\mathbf{D}_{\langle i,j \rangle}$ are the exchange interaction tensor and DM vector between site i and j . \mathcal{A}_i is the single ion anisotropy at site i . In the calculation, we only consider the coupling between nearest neighbors and next nearest neighbors.

As mentioned in the main text, after the coefficients the magnetic effective Hamiltonian is acquired by the four-state mapping approach, it is used in parallel tempering Monte Carlo (PTMC) simulations to study the cycloidal phase. The calculated exchange coefficients and SIA coefficients are shown in Tabs. I and II, respectively.

Practically, it is not possible to perform *discrete* Fourier transformation on the rotated supercell directly, since the lattice vectors \mathbf{a} and \mathbf{b} are not perpendicular to each other, and the primitive cells cannot be discretized into uniform mesh with respect to the lattice vectors. An approximate FT is thus performed as follows. The coordinates of the Fe atoms in a (001) plane of the supercell are first transformed into an infinite plane with basis \mathbf{a}_0 and \mathbf{b}_0 , where the periodicity along the \mathbf{a} and \mathbf{b} supercell lattice vectors is used through the transformation. The discretized coordinates are given within the unit of \mathbf{a}_0 and \mathbf{b}_0 with one of the Fe atoms as the origin. An image could then be created with the values of the x - (or equivalently, y - or z -) component of the spins in a (finite) rectangular range in this plane, to imitate the testing image in the experiments. To reduce the undesirable influence of the periodicity introduced by the image boundary, a relatively large size of 4000×4000 is used.

TABLE I: Calculated exchange parameters and DM interactions (in meV) for Fe-Fe pairs in stretched BFO. The atom positions and distances are given in cartesian coordinates in Angstroms.

	atom 1	atom 2	distance	J_{xx}	J_{yy}	J_{zz}	D_x	D_y	D_z
1	(6.10, 5.93, 1.95)	(6.13, 5.96, 5.86)	3.91	6.152	6.151	6.138	0.029	-0.120	-0.044
2	(2.17, 5.96, 5.87)	(2.14, 5.93, 1.95)	3.91	6.136	6.137	6.122	-0.119	0.031	-0.041
3	(6.10, 5.93, 1.95)	(6.00, 1.99, 1.95)	3.95	5.876	5.863	5.875	0.022	-0.039	-0.101
4	(6.03, 2.01, 5.87)	(6.13, 5.96, 5.86)	3.95	5.910	5.899	5.910	-0.104	-0.044	0.027
5	(2.17, 5.96, 5.87)	(6.13, 5.96, 5.86)	3.96	5.776	5.788	5.789	-0.038	0.023	-0.097
6	(6.10, 5.93, 1.95)	(2.14, 5.93, 1.95)	3.96	5.819	5.830	5.831	-0.046	-0.098	0.026
7	(2.17, 5.96, 5.87)	(6.03, 2.01, 5.87)	5.52	0.180	0.180	0.181	0.001	0.000	0.018
8	(2.14, 5.93, 1.95)	(6.00, 1.99, 1.95)	5.52	0.182	0.182	0.183	0.000	0.001	0.018
9	(2.14, 5.93, 1.95)	(2.07, 2.01, 5.86)	5.54	0.183	0.182	0.182	-0.019	-0.002	-0.003
10	(6.10, 5.93, 1.95)	(6.03, 2.01, 5.87)	5.54	0.174	0.172	0.173	-0.019	-0.002	-0.002
11	(6.10, 5.93, 1.95)	(2.17, 5.96, 5.87)	5.55	0.186	0.187	0.185	0.002	0.019	0.002
12	(6.00, 1.99, 1.95)	(2.07, 2.01, 5.86)	5.55	0.174	0.175	0.174	0.002	0.019	0.002
13	(6.00, 1.99, 1.95)	(6.13, 5.96, 5.86)	5.58	-0.004	-0.005	-0.005	-0.005	0.003	-0.001
14	(2.04, 1.98, 1.95)	(2.17, 5.96, 5.87)	5.58	-0.005	-0.006	-0.006	0.003	0.000	-0.001
15	(2.14, 5.93, 1.95)	(6.13, 5.96, 5.86)	5.59	-0.003	-0.001	-0.003	0.000	-0.003	0.001
16	(2.04, 1.98, 1.95)	(6.03, 2.01, 5.87)	5.59	-0.003	-0.001	-0.003	-0.003	0.005	0.001
17	(2.07, 2.01, 5.86)	(6.13, 5.96, 5.86)	5.66	0.013	0.013	0.015	0.003	0.000	-0.004
18	(2.04, 1.98, 1.95)	(6.10, 5.93, 1.95)	5.66	0.015	0.014	0.016	0.000	-0.002	0.004

TABLE II: Calculated SIA parameters (in μeV) for Fe atoms. The atom positions are given in cartesian coordinates in Angstroms.

	atom	$\mathcal{A}_{yy} - \mathcal{A}_{xx}$	$\mathcal{A}_{zz} - \mathcal{A}_{xx}$	\mathcal{A}_{xy}	\mathcal{A}_{xz}	\mathcal{A}_{yz}
1	(2.04, 1.98, 1.95)	0.7	0.3	-2.7	-0.4	-3.1
2	(2.14, 5.93, 1.95)	0.7	0.4	-2.7	-0.4	-3.1

Then, fast Fourier transformation is performed on this image as usual.

-
- [1] A. Dréau, M. Lesik, L. Rondin, P. Spinicelli, O. Arcizet, J.-F. Roch, and V. Jacques, *Physical Review B* **84**, 195204 (2011).
- [2] J.-P. Tetienne, T. Hingant, L. J. Martínez, S. Rohart, A. Thiaville, L. H. Diez, K. Garcia, J.-P. Adam, J.-V. Kim, J.-F. Roch, I. M. Miron, G. Gaudin, L. Vila, B. Ocker, D. Ravelosona, and V. Jacques, *Nature Communications* **6**, 6733 (2015).
- [3] A. Jenkins, M. Pelliccione, G. Yu, X. Ma, X. Li, K. L. Wang, and A. C. B. Jayich, *Physical Review Materials* **3**, 083801 (2019).
- [4] Y. Zang, C. Di, Z. Geng, X. Yan, D. Ji, N. Zheng, X. Jiang, H. Fu, J. Wang, W. Guo, H. Sun, L. Han, Y. Zhou, Z. Gu, D. Kong, H. Aramberri, C. Cazorla, J. Íñiguez, R. Rurali, L. Chen, J. Zhou, D. Wu, M. Lu, Y. Nie, Y. Chen, and X. Pan, *Advanced Materials* **n/a**, 2105778.